Dynamic behavior of oscillatory plastic flow in a smectic liquid crystal

Richard A. Herke,[1] Noel A. Clark,[1,*] and Mark A. Handschy[2]
[1]*Condensed Matter Laboratory, Department of Physics, University of Colorado, Boulder, Colorado 80309-0390*
[2]*Displaytech, Inc., 2602 Clover Basin Drive, Longmont, Colorado 80503*
(Received 30 December 1996; revised manuscript received 22 April 1997)

Dynamic surface force measurements are used to study the response of a smectic-*A* liquid crystal under layer-normal stress. The smectic *A* is confined in a spherical wedge between crossed cylindrical surfaces having a minimum gap spacing of 0.5–4 μm. The force transmitted between the surfaces by the liquid crystal is measured vs surface spacing using a capacitance micrometer-based surface force apparatus. Above a threshold stress plastic flow results, consisting of individual layers being excluded or included. Each layer flow event has an intriguing dynamical structure, beginning with an enhanced drift rate, which can last for many minutes, accelerating to a rapid separation change of ~1 or 2 s duration wherein the bulk of the relaxation occurs, and tapering off to a background drift rate over a period of a 100 s or more. The single-layer nature of the observed jumps in liquid crystal thickness indicates that they are topological in origin, i.e., slippage events in the phase of the smectic-*A* order parameter that must necessarily involve edge or screw dislocations. A model based on the Glaberson-Clem-Oswald-Kléman helical instability in screw dislocations is the only one found to explain the data, the layering events arising from a cascade of these helical instabilities sweeping radially outward through the smectic-*A* sample. The slow precursor acceleration is due to the nucleation of a few helices in the thin central portion of the sample. As time goes on, the force relieved is transferred to the rest of the sample, pushing larger and larger amounts of the area into the unstable regime, and a type of chain reaction occurs whereby the bulk of a layer is removed. In the end only the material at the edge of the droplet, where the thickness is largest, is left to slowly continue to nucleate, producing a long-term tail.
[S1063-651X(97)10008-3]

PACS number(s): 61.30.−v, 83.50.Nj, 83.70.Jr

I. INTRODUCTION

Smectics *A* are liquid crystal phases having orientational ordering and one-dimensional (1D) translational ordering of rod-shaped molecules. In the absence of applied stress the equilibruim structure has planar layers spaced by the equilibrium period and the local mean molecular long axis, given by the director $\hat{n}$, is oriented along the layer normal, as shown in Fig. 1(a). The 1D stacking structure and the 2D liquidlike nature of the layers combine in the smectic *A* to produce a variety of novel elastic, hydrodynamic, and thermal effects [1]. One of the most exotic smectic-*A* rheological properties is the phenomenon of oscillatory plastic flow: macroscopic samples, in response to the application of a constant rate of layer strain, can exhibit oscillatory layer normal stress [2–5]. Here we present the first study of the dynamics of oscillatory plastic flow in a smectic-*A* liquid crystal.

Oscillatory plastic flow was first discovered in isotropic fluids in measurements of the force transmitted between two closely spaced solid surfaces separated by a fluid layer a few molecules thick [6]. As the surface separation is changed the transmitted force oscillates with a period roughly equal to a molecular diameter. This behavior is a consequence of the layering induced in the fluid by the planar solid surfaces and fluid pair correlations; preferred surface separations correspond to integral numbers of molecular layers between the plates. Whereas in isotropic fluids this induced layer order is short ranged and the consequent force oscillations are confined to the surface region, in smectic-*A* liquid crystals the hybrid 1D solid–2D liquid structure makes oscillatory plastic flow a bulk phenomenon. In the first study of force vs separation for a liquid crystal, Horn, Israelachvilli, and Perez [2]

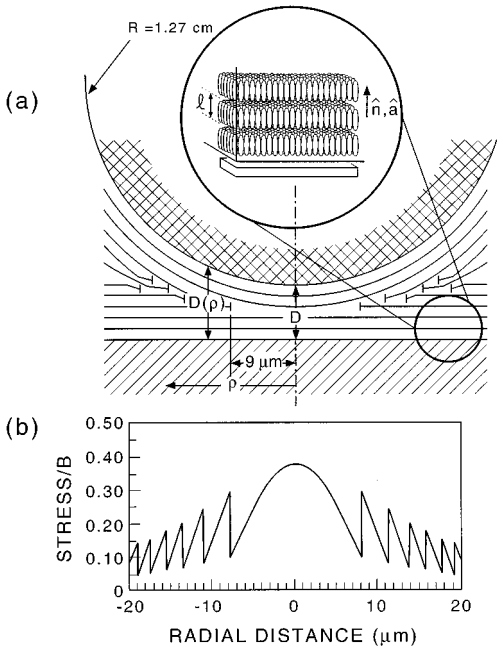

FIG. 1. Sketch showing (a) the position of edge dislocations in the sample, and (b) the state of the stress σ_{33} in the sample under compression.

*Author to whom correspondence should be addressed.

used the Israelachvilli surface force apparatus (SFA) [6] to demonstrate the surface interaction via Frank elastic forces in the nematic phase of the thermotropic liquid crystal 8CB, and found force oscillations in the homeotropically aligned smectic-*A* phase. These oscillations were exhibited by jumps in the separation distance equivalent to one layer thickness. The surfaces were treated for homeotropic orientation (layers parallel to the plates), and the jump size corresponded approximately to the layer spacing of $\delta = 3.17$ nm [7], that is, to integer changes in the number of layers between the plates. The force oscillations became extremely large in magnitude over the last few layers before surface contact and were still detectable even past 2 μm of separation. Other SFA studies on smectics have concentrated on swollen lyotropic smectics *A*—stacks of amphiphilic bilayers separated by a thin sheet of water and swollen by an oil diluent—in which oscillatory forces with the layer spacing were also observed [3]. By using an SFA a modulus of layer compression was directly measured for the first time [4], and the layer bending modulus was extracted [5].

In this paper we present a study of the time dependence of smectic-*A* oscillatory plastic flow, using an SFA based on capacitance micrometry that is particularly well suited for dynamic force vs separation measurements. We find force oscillations out to surface separations of 4 μm; in this macroscopic limit the separation jumps corresponding to the layer number change exhibit an unusual avalanche-type signature, with long gestation periods of gradually increasing acceleration preceding rapid jumps. A variety of models, based on the elastic-hydrodynamic description of smectics *A* [1], were tested to describe these layer-jump events. The only model reproducing the observed dynamic signature is based on the strain-induced helical instability of screw dislocation lines [8,9].

The strain-induced helical instability of screw dislocation lines is a phenomenon unique to fluid smectic liquid crystals and systems that are equivalent under the smectic-*A*–superconductor analogy developed by de Gennes [1]. This analogy is based on the description of an ordered state by the two-component order parameter $\psi(\mathbf{r}) = |\psi(\mathbf{r})| e^{i\phi(\mathbf{r})}$, which in the smectic-*A* case characterizes the layer ordering. For the smectic *A* $|\psi(\mathbf{r})|$ gives the local magnitude of the density modulation associated with the layering, and the phase $\phi(\mathbf{r})$ is such that $\nabla\phi(\mathbf{r}) = \mathbf{n}(\mathbf{r})/l(\mathbf{r})$, where $\mathbf{n}$ is the local layer normal and $l(\mathbf{r})$ the local layer thickness. For continuous deformation of the layers, the net number of layers crossed for integration around a closed loop L, $N = \int_L \nabla\phi(\mathbf{r}) d\mathbf{r} = 0$. In the presence of topological defect lines—edge or screw dislocations in the case of smectic *A*—N need not be zero, but will assume the integral value $N = \beta$ if the loop encloses a defect line of Burger's strength β.

For the experiments described here, the smectic *A* is contained in a gap between molecularly smooth (upper and lower) crossed cylinders, equivalent geometrically to a sphere and a flat plate as shown in Fig. 1(a), each treated to align the molecules normal to its surface (homeotropic alignment). This forces the surface smectic layer parallel to the surface to effectively impose a constant phase $\phi(\mathbf{r})$ over the surface. The integer $N_{AB} = \int_L \nabla\phi(\mathbf{r}) d\mathbf{r}$ counts the number of layers crossed on a path from point *A* on the upper surface to point *B* on the lower surface. If the spacing between the plates is altered, changes in N_{AB} are induced that are necessarily discrete and therefore must be mediated by the generation or motion of topological defects. In our experiments we also observe jumps in separation of size l in response to layer normal compression, indicating that the jumps are topological in nature, involving edge or screw dislocations. Although the nonuniform gap between the cylinders requires the presence of edge dislocations, our analysis indicates that in the macroscopic limit studied here, they are pinned and not involved in the layer jumps in a significant way.

The helical instability of screw dislocation lines was first discovered by Glaberson, Johnson, and Ostermeir [10], who studied the effect of the net fluid flow on quantized vortex lines in superfluid helium II, and by Clem [11], who calculated the response to the applied current of vortex flux lines in a type II superconductor. Quantized vortices in a superfluid and vortex flux lines in a superconductor are the structures corresponding to smectic-*A* screw dislocations in the de Gennes analogy [1]. Glaberson, Johnson, and Ostermeir and Clem showed that at a sufficiently high phase strain, generated, respectively, by flow along the line in the superfluid and by current density normal to the line in the superconductor, equivalent to the strain of the smectic *A*, the linear vortex line becomes unstable. Explicit consideration of this effect in a smectic *A* was first carried out by Bourdon *et al.* [8], who calculated that under either compressive or dilative strain, in a smectic *A*, a previously straight screw dislocation line deforms into a helix to eliminate or add layers, respectively. The fluid layering of the smectic *A* and consequent lack of intra- or interplane shear elasticity makes this a very low energy process, unique among elastic systems to fluid layer smectics. Oswald and Kléman [9] studied the response of very thick smectic-*A* homeotropic samples to large compressive displacements, observing a continuous stress relaxation with a characteristic time that depended in a discrete way on the initial applied stress. They concluded that this behavior was a consequence of the screw dislocation instability, providing our motivation to develop models based on this mechanism to explain the dynamics of layer-jump events probed by direct surface force measurement [12].

II. EXPERIMENTAL APPARATUS

Our surface force apparatus, shown schematically in Fig. 2, is particularly applicable to the investigation of the *dynamics* of the normal force versus distance relationship, employing capacitance micrometry and electronic detection to measure distance, without optical access if necessary [13]. Details of the mechanical and electronic design, components, operation, and performance are available elsewhere [14]. A drop of the sample fluid occupies the space between the two crossed cylinders. The precision screw is electronically controlled and coarsely adjusts the position of the bottom surface to obtain a rough surface separation distance. After coarse positioning the electrostatic clamp locks this surface to a fine control mechanism. The fine motion of each surface is detected capacitively by attaching it to a thin flexible plate, termed a flexure—the top surface directly by an adhesive and the bottom by an electrostatic clamp. The flexure forms the center plate of a three-plate capacitor in a capacitance bridge.

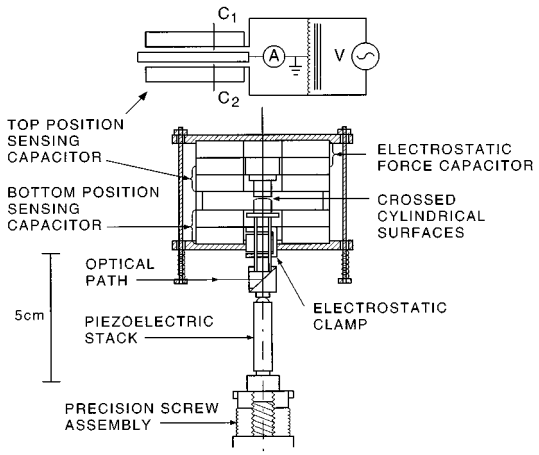

FIG. 2. Schematic diagram of the experimental apparatus showing Blumlein-type transformer ratio bridge and three-plate realization of dual capacitors C_1 and C_2. Windows in the enclosing temperature controlled oven and the 45°-angle mirror near the base provide for optical observations if desired.

The plates are separated by ~ 10 μm gaps. Motion of the surface induces motion of this flexure plate, a consequent change in capacitance, and therefore a change in the unbalance signal from a Blumlein transformer ratio bridge [15], as shown in Fig. 2. Any change in the relative capacitor spacing by motion of the center plate thus changes both the capacitances and the output to the detector. This entire bridge system is termed a capacitance micrometer [16].

The bottom cylindrical surface and capacitance micrometer are connected to a piezoelectric stack for small-scale motion, and the micrometer position is servo controlled to a selected voltage ratio to set the fine position of the bottom surface. Meanwhile the top capacitance micrometer monitors the position of the top cylindrical surface. Beside its role as part of the capacitance micrometer, the flexure plate attached to the top surface serves as a spring. The spring constant then directly relates changes in the position of the top surface to changes in the force between the two surfaces. The whole apparatus is thermostatted to ± 0.02 °C in a temperature controlled oven.

Each capacitance micrometer is sensitive under test to displacements of less than 0.005 nm. Although the sensitivity reached in an experiment is quite good, it does not reach this level because the electronic noise in the piezo servo is $\cong 0.02$ nm, setting an upper limit on the short term sensitivity. Each lone capacitance micrometer drifts in position $\cong 0.1\ \mathrm{nm\ h^{-1}}$, and the total assembly typically indicates drifts between the two surfaces at the rate of $\cong 0.2-0.4\ \mathrm{nm\ h^{-1}}$. Furthermore, once the smectic-*A* liquid crystal sample is placed between the surfaces, these ''drifts'' can grow to 1 or $2\ \mathrm{nm\ h^{-1}}$, depending on the force applied, mechanical relaxation of the sample drop shape, and changes in atmospheric pressure. The error in the absolute accuracy of each capacitance micrometer is $\sim 10\%$. At the force levels employed there is no observable effect of force on drift. The dynamic response time of the force-sensing capacitance micrometer is ~ 0.003 s, essentially controlled by air damping between the flexure and fixed plates. Figure 3 shows that ratio transformer setting changes varied linearly with actual

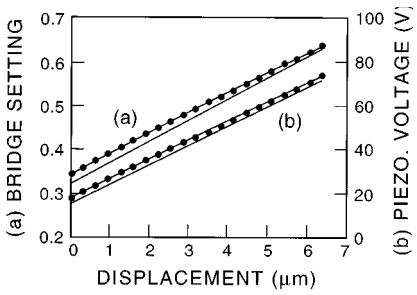

FIG. 3. Calibration tests of capacitance micrometer servo system showing (a) the ratio bridge's transformer setting and (b) the piezo stack's voltage vs the interferrometrically determined displacement.

displacements determined via optical interferometry as well as with the voltage on the piezoelectric stack.

III. OBSERVATIONS: RHEOLOGY OF A THIN HOMEOTROPIC SMECTIC *A* UNDER LAYERNORMAL STRESS

A. Sample geometry and procedure

The sample for these experiments was the liquid crystal 4′-*n*-octyl-4-cyanobiphenyl [8CB or K24], exhibiting isotropic (I), nematic (N), smectic *A* (sm-*A*), and crystal (C) phases [17]. Sample droplets were taken via a syringe from a vial of 8CB purchased from BDH Chemicals/EM Industries and used without further processing. The N–sm-*A* transition temperature of our sample from the vial was $T_{NA}=33$ °C, close to the literature value of $T_{NA}=33.6$ °C [7]. After several months in the SFA it was found to decrease to ~ 31.5 °C, probably a result of water absorption or leaching of ions from the mica.

Filling the SFA was carried out by using the needle of the syringe to touch a drop of 8CB to the two cylindrical surfaces of the assembled apparatus. Capillary action then pulled the sample around the surfaces and into the space between. To the surfaces of the fused silica cylinder were cemented sheets of molecularly smooth mica, each coated with a monolayer of the ionic surfactant hexadecyl trimethyl ammonium bromide to induce homeotropic smectic-*A* alignment. By viewing through two crossed sheet polarizers placed at windows of the outer oven, the inner ~ 1 mm square area of the sample appeared homeotropically aligned, surrounded by unaligned liquid crystal. To first order the surface separation distance $[D(\rho)]$ is that of a sphere and a plate, depending on the distance from the center line (ρ) as $D(\rho)=D_0+\rho^2/2R$, where D_0 is the minimum separation distance at the center line, and the surface radius $R=1.27$ cm as shown in Fig. 7. X-ray diffraction measurements show the period of the smectic layer ordering in 8CB to be $l=3.17$ nm [18]. The layer alignment parallel to the surfaces confines the phase $\phi(\rho)$ of the sm-*A* order parameter to be constant on the upper and lower surfaces at ϕ_{up} and ϕ_{low}, respectively. Since the surface separation varies, either (a) the layer thickness must vary proportionally to enforce $\int_{s2}[\mathbf{n}(\mathbf{r})/l(\rho)]d\mathbf{r} = \phi_{\mathrm{up}}-\phi_{\mathrm{low}}$ or (b) there must be topological defects (edge or screw dislocations) introduced to yield this condition with constant layer thickness. Given the rather extreme sample

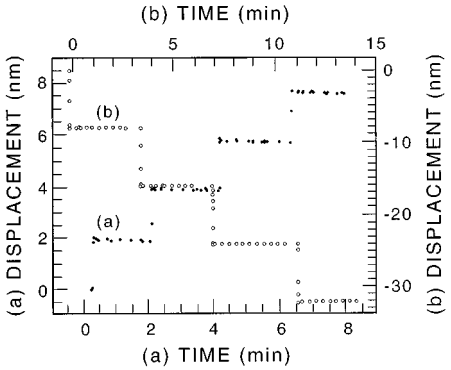

FIG. 4. Response of upper surface displacement to (a) 2 nm lower surface compressive steps at $D_0 = 4\ \mu$m, and (b) 8 nm lower surface dilative steps at $D_0 = 1.4\ \mu$m.

thickness variation (the separation increases by one layer spacing at $\rho = 9\ \mu$m, but within $\rho = 90\ \mu$m the separation increases by more than 100 layers) and the very large stresses necessary to substantially change layer thickness, the most probable equilibrium structure must have edge dislocation loops of the same sort around $\rho = 0$ [Fig. 1(a)].

In general, previous to a data run the piezoservo was used to establish $D_0 = 0$, i.e., bring the lower surface up into apparent ''contact'' with the upper—where the two surfaces began moving in unison even at large forces (the relatively large separations at which these experiments were conducted, in the range of 0.5 μm–4.0 μm, errors due to having a few remnant layers between the surfaces should be negligible). The bottom surface was then lowered, again using the piezoservo set point, to produce the approximate surface separation desired. To leave homeotropically aligned liquid crystal after this procedure [18,19], the surfaces were first pulled apart to a distance a micron or so larger than desired and then compressed to the desired separation.

B. Relaxation event observations

1. Procedure

To observe the oscillatory force jumps noted by Horn, Israelachvilli, and Perez [2], the basic procedure below was followed. First the temperature was set to 26.5 °C, well into the smectic phase. Then the separation distance was set as described above, and the system was allowed to further equilibrate for a day or so. At the beginning of this equilibration period the force on the upper plate could still be as large as ~400 dynes. After the equilibration period the lower surface was raised (or lowered) in increments of 1–8 nm, and the response of the upper surface was observed for a few minutes. This response could be divided into a low force elastic response region and a high force plastic flow region.

2. Elastic response regime

Data collected in the low force, apparently elastic region of the stress vs strain curve is shown in Fig. 4. The plots give the position response of the upper surface to the sudden change in position of the lower surface, for a compression series taken from a position attained after several hours of equilibration at a surface separation of $D_0 = 4\ \mu$m; and a dilation series starting from the force needed to cause plastic flow in compression dropping down to the force needed to again cause plastic flow, but now in dilation at a separation of $D_0 = 1.4\ \mu$m. After each jump in the position of the lower surface the upper moved in unison with it and then remained in place.

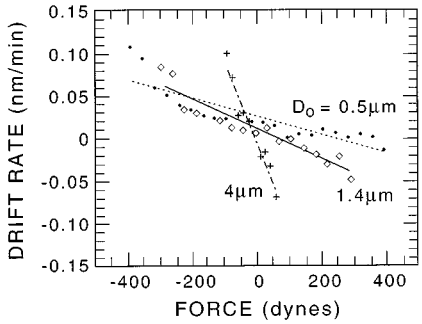

FIG. 5. Linear fits to drift rate vs force data for several values of minimum separation D_0.

The ratios r of the change in the upper surface position to that of the lower surface, $r = \delta x_{\rm up}/\delta x_{\rm low}$, are $r = 1 \pm 0.1$ for $0.5\ \mu\text{m} < D_0 < 1.4\ \mu$m and there is a trend toward an increasing ''stiffness'' of the liquid crystal with decreasing separation distance ($r = 0.9 \pm 0.1$ for $2\ \mu\text{m} < D_0 < 4\ \mu$m). In any case, r clearly indicates that *the effective spring constant of the liquid crystal is an order of magnitude or more greater than that of the spring attached to the upper surface.*

The apparent drift rate in the position readings changed slightly as the force changed. Recall that due to the spring attached to the upper surface, changes in its position also represented changes in the force. Figure 5 displays the rate of drift, found from a linear least squares fit to the displacement data, as a function of the force on the liquid crystal for some different surface separation distances. The data were taken at each distance from roughly the force required to cause plastic flow in compression to approximately that needed to cause dilative plastic flow. The large amount of noise in the data is due primarily to the small number of readings taken at each force and the small size of the drift rate. The drift rate varied roughly linearly with force although the actual slope varied markedly between trials at different separations. Interestingly, however, the total change in drift rate was $\cong 0.1$ nm min^{-1} between the two force extremes in each of these cases. We will show that the linear relationship between force and drift rate breaks down as the force is extended beyond the end points of these curves.

The value inferred above for the effective spring constant of the sm-*A* liquid crystal in turn implies that the edge dislocations in the sample were pinned. In other materials, edge dislocations have been observed under crossed polarizers using the strain-induced (near the dislocation) phase transition from smectic *A* to smectic *C*. The edge dislocations so revealed are ''very irregular because of pinning of their motion'' [20]. Initially, however, this came as somewhat of a surprise because the working assumption had been that the dislocations were free to move and the stress was supported by the central dislocation free region of Fig. 1(a). To see how this assumption is contradicted by the data, one can calculate the effective spring constant ($K_{\rm eff}$) of a cylinder of elastic material with bulk compressibility B and radius $\rho_{\rm max}$ filling the space between the two crossed cylinders and centered at

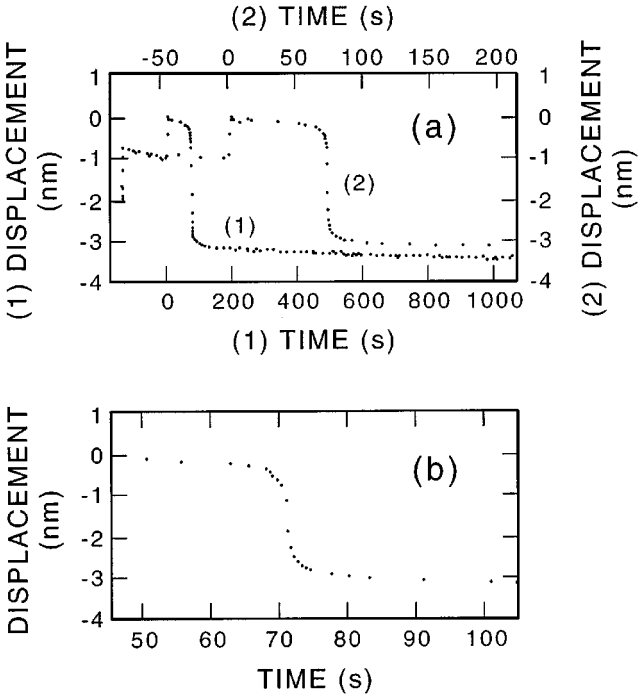

FIG. 6. (a) Response of upper surface displacement to steps in lower surface position near plastic flow threshold, and (b) close up of relaxation jump region ($D_0 = 4.2\ \mu$m).

the point of closest approach. Each ring of material of thickness $d(\rho)$ gives a spring constant contribution of

$$dK_{\text{eff}} = \frac{\delta F}{\delta D_0} = B\,\frac{1}{D(\rho)}\,2\pi\rho d\rho.$$

Integrating over the total cylinder and using $D(\rho)$ as defined previously, the net spring constant comes out to be

$$K_{\text{eff}} = 2\pi RB\,\ln\left(1+\frac{\rho_{\max}^2}{2RD_0}\right).$$

With a bulk compressibility $B \cong 10^8$ dynes cm^{-2} [21] and a minimum separation distance $D_0 \cong 1\ \mu$m, a plug of the liquid crystal $\cong 100\ \mu$m across would be needed to produce a large enough spring constant. However, in this distance the spacing between the cylinders would increase a hundred layer spacings or so, and the sample would contain about a hundred dislocations. If these were not pinned they would move to relieve the stress [22] and produce a much lower effective spring constant.

3. Plastic flow regime

As the force on the liquid crystal increases beyond a certain point, a dramatic change occurs in the character of the response. The smectic-*A* liquid crystal cannot support the total force on it, and a plastic flow occurs. The response curve at the end of a series of compressive steps of Fig. 4 is shown in Fig. 6. The last two 1 nm steps are shown. Following the last step the surfaces again moved in unison. In this case, however, after $\cong 50$ s the upper surface abruptly began dropping, causing a relaxation in the force. Since the lower surface is fixed in position, this drop represents a change in sample thickness. The total event consists of a precursor of slope that is much larger than that before the last compression, a rapid sigmoidal step, and a long tail, adding up to a ~ 3 nm change in sample thickness, or about one smectic layer spacing l. Once such a step occurs another can be generated by additional compression. Following steps to roughly the same threshold force the plastic flow region was again reached and a similar relaxation event occurred. The apparent threshold force could vary greatly between data runs, although it was relatively constant throughout a run. Nearly all of the events had a characteristic sigmoidal displacement in time, but the precise shape and speed of the relaxations varied and was highly dependent on sample and history. However, consecutive events in a compressive or dilative sequence were quite similar. The vast majority of observed events had a size corresponding to one layer or a small integral multiple of layers. Additional example layer relaxation events are shown in Fig. 7. Each plot shows the

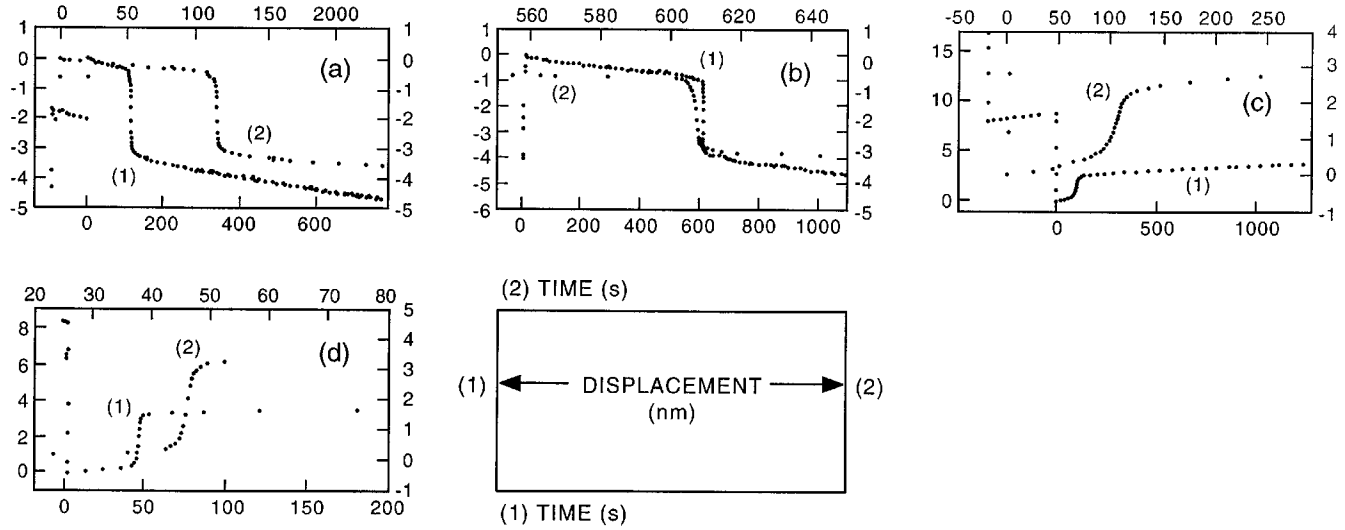

FIG. 7. Response of upper surface displacement to steps in the lower surface position near the plastic flow threshold, (a) $D_0 = 4\ \mu$m, (b) $D_0 = 2.3\ \mu$m, (c) $D_0 = 0.5\ \mu$m, and (d) $D_0 = 1.4\ \mu$m.

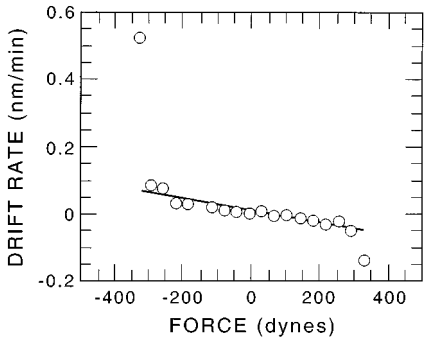

FIG. 8. Example demonstrating the breakdown of the linear relationship between the drift rate and force at extremum force values.

next to the last and the last of the synchronous movements of the upper surface with displacements of the lower, which results in most cases in the following sequence of events.

(i) *Next to the last step*. After the next to the last step the drift velocity (step-slope velocity) is constant in time and commensurate with the solid line in Fig. 8.

(ii) *Initial slow acceleration regime*. After the last step the drift velocity (rate of change of separation) prior to the layering event (preslope velocity) is significantly larger than that between previous steps, now well above the line in Fig. 8, and increases monotonically and slowly over a period ranging from several tens to a thousand seconds, depending on the event; toward the end of this period the acceleration begins to rapidly grow.

(iii) *Sigmoidal jump*. The acceleration divergence culminates in the bulk of the step, which is completed in $\cong 1$ s, and is characterized by a sigmoidal shape in the separation vs time curve and the maximum velocity during the process. The net separation change corresponded well with the smectic layer thickness. It thus appears that one layer was ''squeezed out'' of the sample, or ''sucked in,'' as in the case of Figs. 7(c) and 7(d) which occurred at the end of a dilative series of steps.

(iv) *Relaxation regime*. Following the sigmoidal step is a relaxation lasting several hundred seconds when the velocity relaxes back to its background drift value (postslope velocity), seen between the applied steps leading up to the event.

Table I summarizes some of the basic features of these relaxation event examples and those given in the rest of the paper, giving the separation distance and force at which the data in each figure was taken, the size of each ''layer'' event in a figure, and velocities associated with various portions of each event. The origin of the force has here again been taken to be midway between that required to extrude a layer and that needed to include one. In calculating the size reported for each event the postslope velocity—i.e., the roughly constant drift rate arrived at a few hundred seconds after the main relaxation—has been subtracted from the data, and the event's commencement has been taken to occur at the displacement reached immediately after the final step in the bottom surface position. The estimation of the individual layering event sizes in the multilayer relaxations will be described later. The step-slope velocity was found from a linear least squares fit of the data after the initial bottom surface change. The maximum velocity of each layering event was taken from the slope of a c-spline interpolation over the data. It should be emphasized that these relaxations relieved only a small fraction of the force on the system. Because each relaxation released only about 6 dynes of force, whereas the total force on the samples in the figures varied from about 100–400 dynes, the relaxation released from at most 6% to as little as 1.5% of the total force on each sample.

Besides the main jump these curves also exhibit several other interesting features. Figure 7(a) contains a small $\cong 0.3$ nm ''foreshock'' immediately prior to the main jump. These foreshocks occurred frequently, but rarely without being in close proximity to a relaxation jump, and tended to *immediately* precede a jump. Although they may have triggered the core event, it appears that the relaxation process itself was already well underway by the time of the foreshock occurrence. For example, in Fig. 7(a) there is an obvious increase in the ''linear drift'' about 100 s before the main jump. This

TABLE I. Relaxation event size and slope characteristics.

Figure	D_0 (μm)	Force (dynes)	Size			Step-slope velocity (nm/min)	Preslope velocity (nm/min)	Postslope velocity (nm/min)	Maximum velocities		
			Event 1 (nm)	Event 2[a] (nm)	Event 3[a] (nm)				Event 1 (nm/s)	Event 2[a] (nm/s)	Event 3[a] (nm/s)
7(a)	4.0	1.0×10^2	−3.2	na	na	−0.21	−0.20	−0.12	−1.4	na	na
7(b)	2.3	1.8×10^2	−3.5	na	na	−0.05	−0.07	−0.06	−1.6	na	na
7(c)	0.5	-4.0×10^2	2.9	na	na	0.14	0.47	0.04	0.15	na	na
7(d)	1.4	-3.2×10^2	3.4	na	na	0.13	0.52	0.07	1.6	na	na
11(a)	2.3	1.8×10^2	−3.7	−3.1	na	−0.05	−0.03	−0.01	−2.4	−1.2	na
11(b)	1.3	nm[b]	−3.8	−4.1	na	−0.10	−0.15	−0.05	−1.3	−0.5	na
11(c)	2.3	1.8×10^2	−3.4	−3.1	na	−0.10	−0.15	−0.08	−2.6	−1.1	na
11(d)	1.4	-3.2×10^2	3.9	2.8	na	0.08	0.17	0.03	1.2	0.3	na
11(e)	1.4	3.2×10^2	−4.1	−3.2	−3.5	−0.09	−0.15	−0.02	−1.7	−1.3	−0.3
11(f)	0.5	4.0×10^2	−3.6	−2.7	−1.8	−0.09	−0.14	−0.08	−0.96	−0.35	−0.04
11(g)	1.4	-3.2×10^2	3.3	3.4	2.9	0.17	2.77	0.03	2.2	1.8	0.4
Average			3.4	3.2	2.7						

[a]na: not applicable

[b]nm: not measured

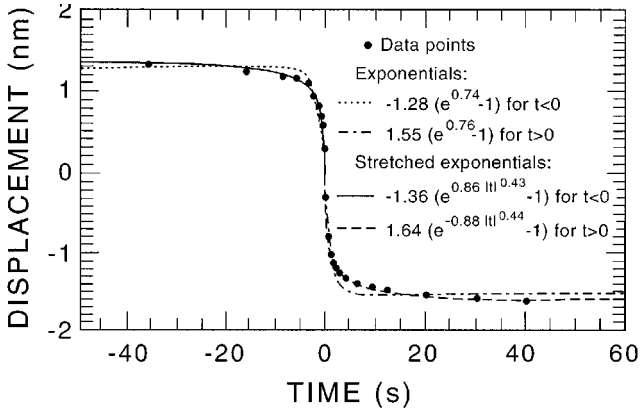

FIG. 9. Exponential and stretched exponential fits to relative displacement during a layer jump.

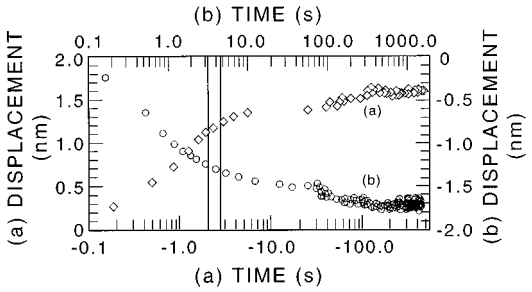

FIG. 10. Log time plot of relative displacement of the two surfaces during a layer jump: (a) before inflection point, and (b) after inflection point, for data of Fig. 7(a) with correction for postslope velocity. This plot shows the wide range of time scales involved in the layer jump events.

is perhaps more clearly displayed in Figs. 9 and 10, the latter of which plots these same data with the postdrift velocity subtracted out and using a $\ln(t)$ time axis with its origin at the inflection point in the center of the step, found by a *c*-spline interpolation over the data. The wide range of time scales required for whole event is evident from this plot. As can be seen, a somewhat enhanced drift was present roughly 100 s before and perhaps 300 s after the main relaxation. Indeed, in general the change in drift rates in Table I between the step-slope, preslope, and postslope velocities are much greater than would be expected from a straight-line extrapolation of curves such as those in Fig. 5. In Fig. 9 the origin has been moved to the center of the event and corrections have been made for the linear postslope velocity. Here the dotted lines represent the best fit to an exponential function and the solid and dashed lines the best fits to the stretched exponential functions shown, chosen because of their extended temporal decay range. Although the change in displacement is very rapid for both, at small times the velocity appears and drops off more slowly in time than an exponential law predicts. For the stretched exponential the time exponent of the fit for $t>0$ in Fig. 9 drops from $\cong 2/3$ if only the initial 10 s are fit, to $\cong 1/3$ if a full 500 s of data are used, giving additional evidence for a broad range of characteristic relaxation times.

The force needed to enter the plastic region and induce a relaxation step tended to increase as the surface separation decreased. Another consequence of decreasing surface separation appeared to be an increasing number of multiple layer relaxations in which two or three layers were removed or included in the sample. Figure 11 gives several examples of multilayer steps at various separation distances. In general, the same basic features were present as in the single-layer relaxations [note the foreshock in Fig. 11(b)], but the total relaxation was some multiple of the single-layer spacing, and *between each ''single'' layer event, although the relaxation rate slowed precipitously, it typically remained much greater than the background drift.* These lulls between events had durations of only a very few seconds [Fig. 11(e)], tens of seconds [Figs. 11(b) and 11(c)], or even past a 100 s [Fig. 11(f)]. For the purposes of Table I, the end of one layering event and the beginning of another were taken to occur at the minimum in the magnitude of the slope of a *c*-spline interpolation over the data in such a lull. Perhaps the most interesting feature beyond what was seen in the single-layer events was the strong dependence of the relaxation speed on the relaxation force. The maximum rate of separation change deduced from a *c*-spline interpolation on each layer event of the figures is also shown in Table I. For example, in Fig. 11(e) the relaxation of two layers accounted for only about a 4% change in the total force. However, the change in the maximum rate of displacement in the second event was nearly an order of magnitude slower than that of the first. Therefore it seems evident that these relaxation steps were threshold-related phenomena not only in their initiation but also in their time development.

IV. THEORY AND COMPUTER SIMULATION

Although the details of the relaxation events display a great deal of variation, they also exhibit common features including: (1) a size equivalent to a small integer number of layers, (2) a similar shape in time, (3) the existence of an apparent critical induction force, and (4) a highly nonlinear dependence of the speed of the relaxation on the force. The shape of each relaxation event generally includes an initial enhanced ''drift'' rate, which can last for minutes, followed by an acceleration in the surface separation change over several seconds leading to a period typically of only 1 or 2 s duration in which the bulk of the relaxation occurs, and ending in a tail wherein enhanced relaxation motion is detectable for around 100 s or more.

The beginning point for explaining events that discretely alter layer number is their fundamentally topological (edge or screw dislocation) nature. Attempts to model the events based on edge dislocation motion, however, have led to little success. A more successful model involves screw dislocations passing from one of the two cylindrical surfaces to the other, and a helical instability they can exhibit on the smectic-*A* phase under stress or, stated more correctly, under dilation. Although these screw dislocations are not geometrically necessary, they have a low energy of creation—zero, in fact, ignoring the core energy—and should be numerous in the sample [23]. Like edge dislocations they have been observed in the polarized light microscope near the smectic-*A*–smectic-*C* phase transition [24], and they have been observed using freeze fracture etching methods in the $L\alpha$ phase of lecithin at densities of $\cong 1\ \mu m^{-2}$ [25]. Under compression (dilation) the straight screw dislocation line can helix with

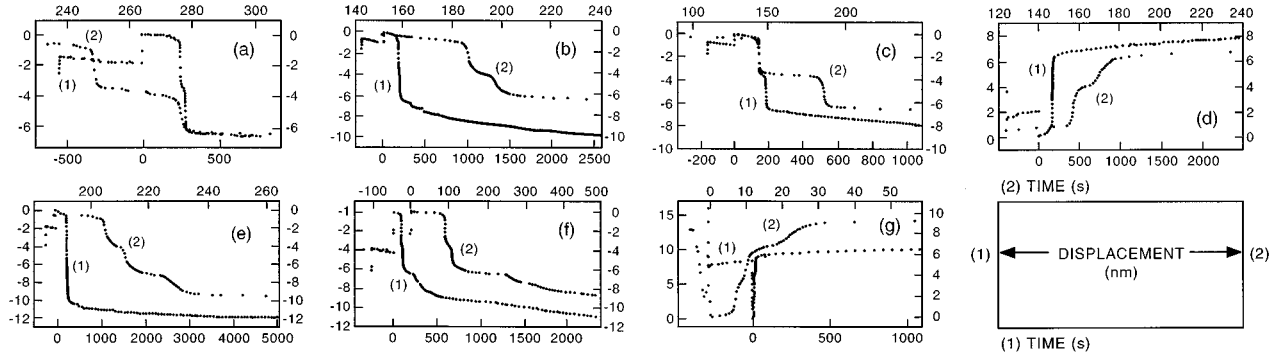

FIG. 11. Response of upper surface displacement to steps in lower surface position near plastic flow threshold: (a) $D_0=1.4\ \mu$m, (b) $D_0=1.3\ \mu$m, (c) $D_0=2.3\ \mu$m, (d) $D_0=1.4\ \mu$m, (e) $D_0=1.4\ \mu$m, (f) $D_0=0.5\ \mu$m, and (g) $D_0=1.4\ \mu$m.

one or more layers of liquid crystal being excluded (included) in the area encompassed by the helix. It is proposed that the observed relaxation steps are the result of a cascade of these helical instabilities of layer-jump events in the screw dislocations populating the smectic-*A* liquid crystal sample. Computer simulations based on this assumption fit the observed phenomena well.

A. Edge dislocation model

As stated, the first attempts to explain the relaxation events focused on the geometrically necessary edge dislocations populating the sample. Figure 1(a) gives an idealized cutaway view of the liquid crystal sample between the cylindrical surfaces. The dislocations in the diagram are actually parts of roughly circular loops. There are four factors controlling the motion of these dislocations. The first is the stress applied to the liquid crystal. The contribution of this factor has been developed by Pershan [26] whose results are summarized below. Figure 1(b) shows a possible state of the 33 elements (3 denoting the layer normal axis) of the stress tensor σ_{33} through the sample taken to be under a slight compression. The stress increases at each dislocation with the size of the jumps, and the absolute magnitude of the stress is inversely proportional to the sample thickness $[D(\rho)]$ at the radius ρ. Letting N_0 be the number of layers at the center line of the sample, n the number of layers added by dislocations at radii $<\rho$, δ the equilibrium layer thickness, and B, the bulk compressibility, the stress can be written,

$$\sigma_{33}=B\left(\frac{(N_0+n)l-D(\rho)}{D(\rho)}\right).$$

The stress tensor element at the dislocation is taken to be the average of the stress given by the above at ρ just smaller and larger than the dislocation radius. The force on the dislocation line per unit length $\mathbf{f}_\sigma$ depends on line density $\mathbf{j}_d$ and stress field $\mathbf{\Phi}$ as

$$\mathbf{f}_\sigma=1(\mathbf{j}_d\times\mathbf{\Phi})=f_{\sigma 2}=b\Phi_3\sin(90°), \tag{4.1}$$

the Peach-Koehler equation for the force on a dislocation in a solid [26]. Taking $\sigma_{33}=-\mathbf{\Phi}_3$, the force on the dislocation line is

$$f_{\sigma 2}=bB\left(\frac{2[(N_0+n)l-D(\rho)]-1}{D(\rho)}\right).$$

This result ignores inter dislocation forces, which are negligible when the dislocations are forced to the sample midplane, as they should be in this case [26,20]. Viscous drag (f_ν) from the surrounding liquid crystal is a second force acting on an edge dislocation line [30,27]. The drag is proportional to the velocity of the dislocation line and depends on the mobility (μ), which in turn is a combination of the liquid crystal viscosity (ν), and the permeation distance (κ^{-1}). This drag component has the form

$$f_\nu=\frac{b}{\mu}\frac{dr_e}{dt}=-(\nu\kappa)b\frac{dr_e}{dt},$$

where r_e is the radius of the edge dislocation line. Thirdly, there is the force (f_γ) due to the line tension (γ), which will oppose the growth of a dislocation and is given by the usual equation [30] $f_\gamma=\gamma/r_e$. This, along with the stress force, also controls the nucleation of new edge dislocations in the smectic. If an edge dislocation of a certain radius is spontaneously generated, it will grow only if the stress force is large enough to overcome this line tension force. Otherwise, it will collapse in upon itself. Finally there are pinning forces which hold the dislocations [21] in place at low force levels. No real theory of these exists since they can have any number of sources, including impurities, surface irregularities, and other defects [28]. The computer simulations employed

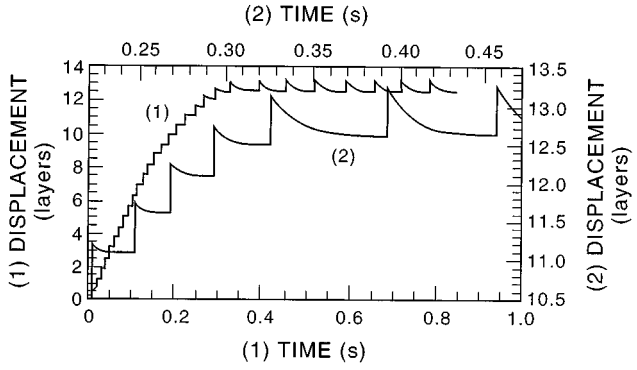

FIG. 12. Results of the edge dislocation computer model.

TABLE II. Geometrical and liquid crystal 8CB parameters used in the computer simulations.

B (Ref. [21])	1.8×10^{8} erg cm^{-3}
l	3×10^{-7} cm
b	3×10^{-7} cm
μ (Ref. [27])	10^{-7} cm^2 s gm^{-1}
γ (Ref. [26])	$\sim Bb^2=1.6\times10^{-5}$ erg cm^{-1}
r_{th}	1×10^{-4} cm
σ_c	1.8×10^{5} dyne cm^{-2}
N_0	500 layers
D_0/l	499 layers
k_{sp}/k_{LC}	0.1
K (Ref. [31])	8×10^{-7} erg cm^{-1}
$\lambda=(K/B)^{1/2}$	6.67×10^{-8} cm
r_c (Ref. [9])	3×10^{-7} cm
e_c (Ref. [9])	$\sim0.2Bb^2=3.2\times10^{-6}$ erg cm^{-1}
μ_h (Ref. [27])	10^{-7} cm^{2}s g^{-1}
R	1 cm
T	299.5 K

two different, simple models. The pinning force in both was taken to have a frictional character with a maximum magnitude σ_c. In one, this was true for both a static and moving dislocation line, and in the other, to somewhat simulate the cloud of impurity [29] theory of dislocation pinning in solids, this was true for a static line but the pinning force was assumed to drop to zero for a moving dislocation.

An example of the results from molecular dynamics simulations carried out with these ideas and forces is shown in Fig. 12. In these simulations, as in the experiment, the force on the sample is increased in increments and the response of the simulated top surface is observed. Nucleation of new edge dislocations takes place when the stress force in the middle of the smectic-*A* liquid crystal droplet exceeds that of the line tension on an edge dislocation loop with some threshold radius r_{th}, and all the dislocations are allowed to respond to the various forces on them. The particular simulation of Fig. 12 incorporated 2000 edge dislocations initially placed at their equilibrium positions and pinned with the first, static plus dynamic frictional force case, mentioned above. The simulated bottom surface is raised in 0.7 layer $\cong$2 nm increments. Other parameters for the simulation are as shown in Table II.

The general features exhibited in Fig. 12 are relatively independent of the exact parameters used, which basically affect only the time and force scales involved. At low force levels the top surface simply moves in step with the force increment by an amount depending on the ratio of the top surface spring constant (k_{sp}) to the effective spring constant of the liquid crystal (k_{LC}). Subsequent to reaching a certain ''critical'' value, however, after the initial response to the stress, the top surface begins to drop. At this point the stress in the center has grown large enough to either nucleate new defects or unpin some of the existing inner ones. Those on the edge are still pinned. Eventually the force grows to a point and the dislocations have adjusted themselves so that any increase in the force leads to the unpinning of all the dislocations and the decay of the top surface back to its position before the last force increment. Although a type of critical force value for plastic flow is exhibited, the simulated steps have qualitatively the wrong form, being more of an exponential decay. Also, instead of having the characteristic integer layer size, they depend *strongly* on the force increment. This failure is intrinsic in the edge dislocation picture, stemming chiefly from the linear dependence on stress of the force on the edge dislocations in an experimental geometry that compels the stress to change radically through the sample volume. *As a result, the nucleation of new edge dislocations can occur* only *at the high stress center line of the crossed cylinders and this is the only mechanism available to impose the layer sizing on the relaxation events. At the same time, however, the majority of the force is not carried in the center but by the sample farther out in the lower stress region. This combination intrinsically prevents nucleations of new edge dislocations from determining the event size, and will rarely lead to steps that are of layer (or multiples) thickness*. It is difficult to envision reasonable modifications to the model that can overcome these problems. However, the edge dislocation picture may be relevant in ultrathin samples of small overall radius, where the center dominates the force [2–4].

B. The helical instability of screw dislocation cascade model

Given the topological nature of the step events and the elimination of edge dislocations to explain relaxation steps, the role of screw dislocations was investigated. In very thick samples of 8CB under high stress [9], screw dislocations offered a promising mechanism. It was discovered that the time constant of the exponential decay to equilibrium of 8CB in the smectic-*A* phase placed under a large stress unexpectedly varied with the stress, becoming shorter as the stress became larger [27]. Oswald and Kléman found that helical instabilities in screw dislocation lines provided an adequate explanation for their data [27]. They even suggested that these might be related to other puzzling phenomena [30] found in smectic-*A* flow investigations, including the work of Horn, Israelachvilli, and Perez [2] which stimulated the present study.

A schematic diagram of a (left-handed) screw dislocation in the smectic layering [23] is shown in Fig. 13(a). The helical instability of screw dislocations is a mechanism whereby, in response to an external force tending to reduce (increase) the layer thickness, the smectic *A* can expel (add) a layer or layers [8]. The initial screw dislocation line is assumed to run vertically between two horizontal boundary surfaces separated by a distance D to which it is firmly attached [Fig. 13(a)]. Under stress the new shape of the dislocation is a helix of radius r and with

$$z=\frac{D}{p}\frac{\theta}{2\pi},$$

where D/p is the helix pitch and the pitch parameter p is a positive integer for right-handed helices and a negative integer for left-handed helices [Fig. 13(b)]. This alteration in the screw line shape can occur because it lowers the stress in the sample. If the helix and the screw dislocation have the same

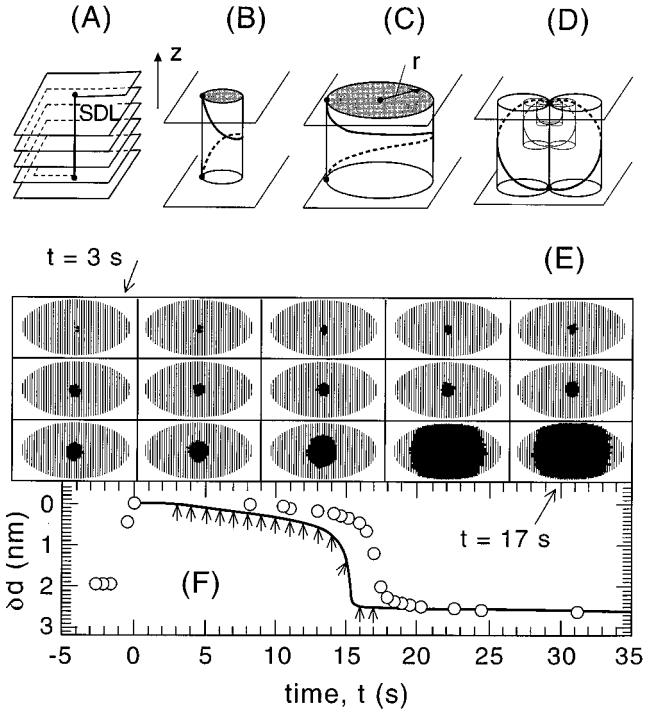

FIG. 13. (A) Smectic-*A* screw dislocation line (SDL). The order parameter phase advances by 2π with each circuit around the core (vortex line). (B) Helixing instability of the screw dislocation under compressive stress. One layer is removed between the plates in the shaded area. (C) As the radius r of the helix grows, the line rotates toward the layer plane, becoming more like an edge dislocation. (D) Helix SDL pairs generated by stress. (E) Simulated time evolution of a single-layer squeezing-out event arising from a helixing avalanche in a 25×25 SDL array after a compressive step $\delta d = -84.6$ Å at $t=0$, showing lattice configurations at 3–17 s corresponding to the times indicated by the arrows in (F). The helixed SDLs (black area of increasing size) appear first near the center ($\rho=0$), initially increasing slowly in number and producing a slowly decreasing sample thickness [δd in (F)]. The decrease in d enhances the probability that remaining SDLs will helix, leading to an outward traveling wave of helixing and a jump in δd. (F) The $\delta d(t)$ for the simulated event in (D). The curve of open circles depicts an experimental layer squeezing-out event at $d_{\min}=4\ \mu$m. For this simulation, $d_{\min}=4\ \mu$m, $p=1$, $n=1$, $\rho_{\min}=0.8$ mm, and $\rho_{\mathrm{maj}}=1.6$ mm.

handedness then the helical shape removes a number of layers proportional to p from the cylindrical volume of radius r inside the helix. Conversely, if the directions are opposite, then the layers are added to the interior of the helix. Reference [14] sketches an heuristic argument visualizing this addition or subtraction of layers.

Although it is assumed that a screw dislocation line already exists in the sample, it is not difficult to envision scenarios whereby the stress itself can nucleate new screw dislocations from the bulk. For instance, every vertical line through a perfectly ordered liquid crystal can be thought of as consisting of both a left -and right-hand screw dislocation superimposed on one another. Stress would tend to make one of these helix in a clockwise direction and the other in a counterclockwise manner. In this way, the stress might peel apart two ''virtual'' screw dislocations, as pictured in Fig. 13(d).

As the helix grows, the line orientation of the screw dislocation becomes more parallel to the liquid crystal layers and perpendicular to the vertical Burgers' vector, which can be seen by comparing Figs. 13(b) and 13(c). The screw orientation thus takes on the character of an edge dislocation, and as the edge character becomes more pronounced, in all probability the repulsive image forces of the boundaries will push the coils of the line into the center where, through a not well understood nonlinear process, the loops will pinch off to form an edge dislocation surrounding a once again straight screw dislocation. The characteristics of the *generation* of step events via the screw dislocation instability, however, are very different than that via edge dislocation motion. While the direct nucleation of edge dislocations depends on the *stress* in the sample, the nucleation probability of the helical instability rather depends strongly on the absolute *dilation* of the sample and therefore *only weakly on the sample thickness*, making it possible for the entire sample to be on the brink of nucleating the helices. The slow dependence on sample thickness will cause the center to nucleate at a slightly lower dilation than the outer edges of the sample. However, the stress or strain relieved in the center will then be transferred outward increasing strain at the edge and possibly causing these screw dislocations to become unstable. Thus it is conceivable that the relaxation step instabilities are actually the result of a wave of helical instabilities of the screw dislocations moving radially outward through the sample.

Based on the methods of Kléman [23], Bourden *et al.* [8] calculated, assuming a linear elasticity, the energy of a helical screw dislocation in a homeotropic smectic-*A* sample with a thickness D, whose boundaries have been displaced a total distance a from an equilibrium unstrained position. The value a is taken to be positive when the strain is dilative. They found three contributions to the energy that depend on the helix of the screw dislocation. One is simply the total core energy, which is proportional to the length of the dislocation. Since the length of a helix whose radius r is small compared to its pitch (D/p)

$$L \approx D\left(1+\frac{2\pi^2 r^2 p^2}{D^2}\right),$$

the dependence of the core energy on the helix can be written

$$W_c = e_c(\delta L) = e_c\left(\frac{2\pi^2 r^2 p^2}{D^2}\right),$$

where e_c is just the core energy per unit length. This is quadratic in p and thus always positive and opposing the growth of the helix. There is also a contribution from the self-energy of the helical line, which can be written

$$W_s = \frac{b^2 K}{\lambda}\frac{r'^2 p^2}{4}\int_0^{k_c'} dk' \int_0^x du\ \frac{\cos 2pu}{\sinh k'\pi} \times J_0(2\sqrt{k'\pi}r'\sin pu)\left(u\ \cosh k'u - \frac{\sinh k'u}{k'}\right), \tag{4.2}$$

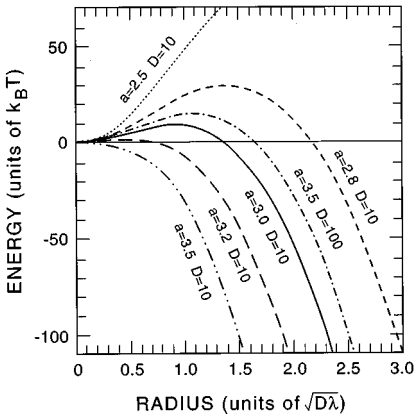

FIG. 14. Total helix energy dependence as a function of the reduced radius $r'=r/(D\lambda)^{1/2}$ for various values of dilation a in units of number of layers and separation distance D in μm.

and must be integrated numerically. Here, once again K is the liquid crystal splay elastic constant, B is the liquid crystal bulk compressibility, and the characteristic length $\lambda=(K/B)^{1/2}$. The helix radius (r) is given in a dimensionless form $r'=r/(D\lambda)^{1/2}$, and k' is also a dimensionless parameter equal to $D\lambda q^2/\pi$ with q being a reciprocal length in the plane perpendicular to the screw dislocation line. The upper limit on k' is set by the core radius (r_c) as a cutoff value $k_c'=4\pi D\lambda/r_c^2$. W_σ is always positive and thus opposes any growth in the helix. The last contribution to the energy of the helix comes simply from the change of the stress in the liquid crystal over the area occupied by the helix. Generally this contribution can be either positive or negative depending on the relative helicities of the screw dislocation and the helix and the sign of the stress. However, since the other two contributions are positive, this contribution must be negative for the helix to appear and grow. Since, as seen earlier, a helix of the same direction as the screw dislocation removes a layer or layers from the interior of the helix, this will be the case in compression. Similarly, in dilation the helix and screw will have opposite helicities, causing an increase in the number of layers inside the helix. In either case the resulting energy is $W_\sigma=-|p|\pi r^2(B|ab|/D)$. Like W_c (and W_s to first order) this is quadratic in the radius and inversly proportional to the liquid crystal thickness.

The total energy is $W_T=W_c+W_s+W_\sigma$. Plots of W_T for a pitch parameter $p=1$, with respect to the dimensionless radius r' are shown in Fig. 14 for various changes in sample thickness, dilation a, and plastic separation D. There are three broad categories for the total energy of the helixed screw dislocation line. At small values of the dilation, such as when the core energy dominates the stress energy, the total energy is always positive and no helix can ever grow. At relatively large values the stress energy dominates for all radius values and a helix immediately forms and grows. What is of particular interest, however, is the case of moderate dilation magnitudes. In this case the core plus self-energy dominate at low values of the helix radius but the stress energy dominates at higher values. Thus, the energy as a function of radius first rises, reaches a maximum value, and then drops, creating an energy barrier to the creation of a helix. As can be seen, the size of this energy barrier $W_{\max}$ is a very strong function of dilation a. Meanwhile it is a much weaker function of the sample thickness D, an order of magnitude change being roughly equivalent to only a half a layer change in the dilation. The energy barrier also depends on the pitch parameter. Since W_c and W_s both depend quadratically on p, whereas the stress energy W_σ has only a linear dependence, helices with more than one loop have significantly higher activation energies and can be ignored.

For such an activated process, the probability per unit time for the formation of a helix is estimated to be

$$P_t=\omega_1\exp\left(\frac{W_{\max}}{k_BT}\right), \tag{4.3}$$

where ω_1 is the screw line natural vibrational frequency and k_B and T are Boltzmann's constant and temperature [31,8]. As in the case of solids, it is assumed that the line vibrational frequency will be roughly that of a string with the same length D, mass per unit length $\cong\rho_{\rm LC}b^2$, and tension as the screw dislocation. This tension is approximately $\tau_s=(dW_s)/(d\delta L)$. This derivative is seemingly difficult to obtain since W_s must in general be found numerically. However, in the small radius limit the integration can be done analytically [9]. In this case the Bessel function to first order is equal to 1, and the resulting approximation for the self-energy is

$$W_s\approx Bb^2\,\frac{\pi^2}{4}\,p^2\,\frac{r^2}{D}\ln\frac{2\pi D\lambda}{pr_c^2}.$$

The tension is then

$$\tau_s\approx\frac{Bb^2}{8}\ln\frac{2\pi D\lambda}{pr_c^2},$$

and the result for the line vibrational frequency is $\omega_1\approx(1/D)\sqrt{\tau_s/(\rho_{\rm LC}b^2)}\sim(1/D)\sqrt{B/(\rho_{\rm LC})}$. Once the helix is nucleated, the helixed dislocation line experiences an outward force due to the applied stress, and a balancing inward force due both to line tension and viscous drag. The line is assumed to be in dynamic equilibrium at its instantaneous terminal velocity. The outward stress-induced force is just the Peach-Koehler force [see Eq. (4.1)]. Letting $\tilde{D}$ be a reduced distance equal to $D/(2\pi p)$ and Φ the angle made with the original screw dislocation line, this force is given by

$$F_\sigma=\sigma b\,\sin\Phi=\sigma b\,\frac{r}{(\tilde{D}^2+r^2)^{1/2}}. \tag{4.4}$$

The inward viscous force is simply $F_v=-(b/\mu_h)(dr/dt)$, where μ_h is the helical line mobility. The other inward force depends on the line tension, which is taken to equal $T_1=(\partial/\partial\delta L)(W_c+W_s)=e_c+\tau_s$, and gives a force of $F_T=(T_1/R_h)=(T_1r/(r^2+\tilde{D}^2)$, where R_h is the helix radius of curvature. Thus the equation of motion for the helix line then takes the form

$$\frac{b}{\mu_h}\frac{dr}{dt}=\sigma b\,\frac{r}{(\tilde{D}^2+r^2)^{1/2}}-\frac{T_1r}{\tilde{D}^2+r^2}. \tag{4.5}$$

C. Screw dislocation instability cascade-based models of layer-step events

1. Computer simulation

In order to probe the possible role of the helical screw dislocation instability in the observed relaxation events, several different Monte Carlo–based computer simulations of the geometry and experiment have been carried out. In the simulations the ragged drop of smectic-*A* liquid crystal is approximated by a droplet of elliptical area with major and minor radii $\rho_{\max}$ and $\rho_{\min}$, of thickness given by $D(\rho) = D_0 + (\rho^2/2R)$. Superimposed on the droplet is a rectangular lattice of points, each rectangular unit cell having the same aspect ratio as the ellipse. A spring of spring constant $K_{\rm sp}$ compresses (dilates) the sample working against the liquid crystal effective spring constant $K_{\rm LC}$. In analogy with $K_{\rm eff}$, $K_{\rm LC}$ is calculated from a sum over the lattice points lp,

$$K_{\rm LC} = \sum_{\rm lp} \frac{1}{D(\rho_{\rm lp})},$$

and $K_{\rm sp}$ is taken to be a certain fraction of this. In general this fraction is set such that the percent release of force per layer event is typical of what was found experimentally.

In order to reduce computation time the state of each unit cell is taken to be represented by that within a ''pinning'' radius $\rho_{\max}$ of the cell lattice point. Thus a small area around each lattice site is simulated, and the results are taken to apply to the entire unit cell. If, in the course of the simulation, a layer is removed from this area around a particular site it is assumed that a layer has been removed from the entire cell surrounding this site. The exact ''pinning'' radius itself is another adjustable parameter representing the size to which a helixed screw dislocation line can grow before becoming pinned, and it is implicitly assumed that the helices in general do not cross. Pinning occurs in the actual liquid crystal sample since as the helix grows it comes to have more and more of an edge dislocation character and the edge dislocations themselves are pinned. Furthermore, neighboring helices could effectively pin each other. At small radii, Eq. (4.4) indicates the driving force behind the helix growth is small and would be stopped by the reduction in stress accompanying an encounter with another helix.

In the simplest form of the model, each lattice site is assumed to be the location of a latent screw dislocation line. The probability per unit time of each individual screw dislocation helixing is given by Eq. (4.3), and the nucleation radius is assumed to be greater than $\rho_{\max}$. In other words, a layer is supposed to be immediately removed from the particular unit cell once the helix nucleation occurs. After each time step, the stress relieved at any nucleated positions equal to $1/D(\rho_{\rm lp})$ is then transferred to the rest of the system, changing the compression in units of layers by an amount depending on the two spring constants as

$$\delta\alpha = \frac{1/D(\rho_{\rm lp})}{k_{\rm LC}} \frac{k_{\rm LC}}{k_{\rm LC}+k_{\rm sp}}.$$

The process is then repeated. In general, the time step length is adjusted to keep the maximum nucleation probability below 50%. For the steepest jumps, however, this has proven impractical with respect to computational time and the step size is not allowed to drop below a minimum of 0.01 s. As a rule of thumb, these portions of the simulation roughly correspond to those portions of Fig. 15 in which individual simulation points can be discerned. These sections would thus be even steeper than pictured if an infinitesimal time step were used. At the nucleated positions the compression has effectively been lowered by one layer and thus the probability of another nucleation is exceedingly improbable. At those positions that have not yet nucleated, however, the increased compression boosts the nucleation probability. Figure 13(f) shows the results of such a simulation in which the sample has been initially compressed by 2.665 layers. The progression in Fig. 13(e) is a time series of the nucleated sites corresponding to the marked points on the solid line of Fig. 13(f), which displays the displacement as a function of time. The open circles are typical experimental data for comparison. As can be seen, initially due to the slight dependence of the energy on thickness the helices begin to nucleate in the center. The result is a slowly accelerating change in the displacement. As the compression on the unnucleated screw dislocations increases due to the extreme dependence of the helix nucleation probability on this compression, the helixing becomes more and more rapid, yielding a very rapid jump. In the end nearly all the dislocations have nucleated except those at the far edge where the sample thickness is very large. These continue to slowly nucleate giving rise to a slowly decreasing tail. Comparison with the data shows that all the major experimental features are present. Furthermore, the implied change in surface separation of around five layers, that is, twice the initial dilation necessary to go from including to excluding a layer is consistent with the values found in Table I.

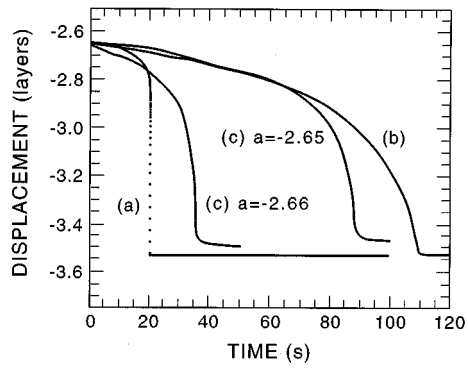

FIG. 15. Simulation of the single-layer relaxation event, (a) $\rho_{\min}=\rho_{\max}=1.0$ mm; (b) $\rho_{\min}=\rho_{\max}=1.4$ mm with $D_0=4\ \mu$m, $k_{\rm sp}/k_{\rm LC}=0.12$; and (c) $\rho_{\min}=1.0$ mm, $\rho_{\max}=2.0$ mm, $D_0=4\ \mu$m, and $k_{\rm sp}/k_{\rm LC}=0.12$, showing dependence on initial dilation a (in layers).

Figure 15 demonstrates the rather strong dependence of the dynamics on droplet size. The rapidly occurring event is simulated using a circular droplet of 1 mm radius, whereas the much slower relaxation occurs with a 1.4 mm droplet. As with the actual data, compare, for instance, Figs. 15(a) and 15(b) with Figs. 7(c) and 7(d), although the exact dynamics are variable, within reasonably large limits the qualitative features remain the same. Notice that these plots do not have a tail at the end of the relaxation since the droplets are not large enough for the dislocations at the edge to require a

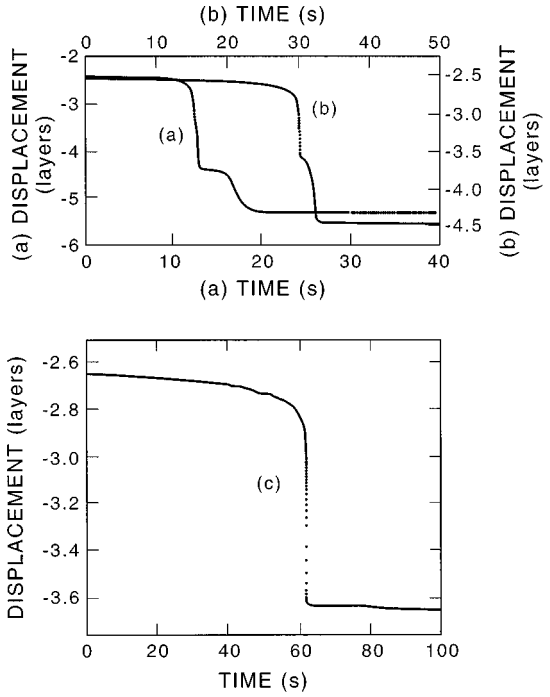

FIG. 16. Simulation of multilayer relaxation events with (a) multiple nucleation probability (MNP)=11.25% and ρ_{min} =0.9 mm, ρ_{max}=1.8 mm, D_0=2.5 μm, and k_{sp}/k_{LC}=0.08, and (b) MNP=11.25% and ρ_{min}=0.8 mm, ρ_{max}=1.6 mm, D_0 =1.5 μm, and k_{sp}/k_{LC}=0.04; and (c) simulation of the single-layer relaxation event with MNP=11.25% and ρ_{min}=1.0 mm, ρ_{max}=2.0 mm, D_0=4 μm, and k_{sp}/k_{LC}=0.12.

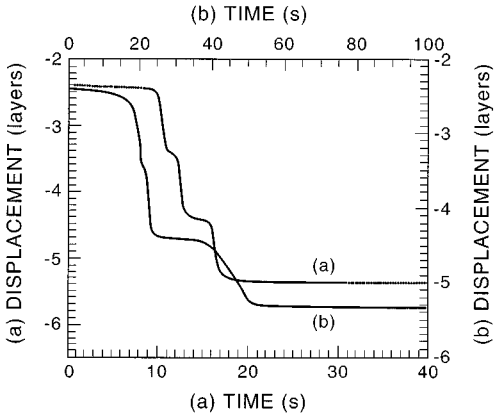

FIG. 17. (a) Simulation of three layer event including dynamical growth of helices with $\int_{max}$=0.5 μm and MNP=12.5%, ρ_{min} =0.4 mm, ρ_{max}=1.15 mm, D_0=1.5 μm, and k_{sp}/k_{LC}=0.04. (b) Simulation of three layer event with dynamical growth and spontaneous generation of screw dislocations creating constant equilibrium density of $\pi/4/\mu m^2$. Also r_{max}=0.5 μm and MNP=10%, ρ_{min}=0.7 mm, ρ_{max}=1.4 mm, D_0=1.5 μm, and k_{sp}/k_{LC}=0.04.

dilation more than one layer greater than that taken to nucleate those at the center. However, if a circular droplet is made large enough to exhibit such a tail the other dynamical features become much too slow. For this reason, and because there is no rationale to expect the real liquid crystal samples to approach anything near a perfect circular shape, elliptical droplets are usually assumed. Figure 15(c) shows the large variation that can occur in the ''starting time'' of the jump due to differences in the initial dilation. Here the bulk of the relaxation is delayed by more than a factor of 2 due to a change in the initial dilation of only a minor fraction of a layer.

In general, the procedure outlined above, which basically reproduces the single-step events, does not produce any multistep events. The reason for this is that at the ''end'' of the first step the unnucleated large radii screw dislocations and the reduction of restoring force of the spring combine to lower the compression on the sample. Thus the probability of any further nucleations in the center of the sample are greatly reduced. In order to reproduce multistep events, a limited multiple nucleation percentage (MNP) $\cong$10%, of nucleations are allowed to induce another nucleation at the same location. In the real sample, perhaps after a helixing screw dislocation ''pinches'' off, leaving an edge dislocation surrounding a screw dislocation line, the screw dislocation is not straight but distorted, yielding a higher nucleation probability. Or possibly there is some crossing of dislocation lines, which would effectively lead to the equivalent situation. In any case it is postulated that some mechanism exists for removing more than one layer at a time from a small portion of the sample. Simulations done under this assumption are shown in Fig. 16. The results in Fig. 16(c) are similar to those in Fig. 15(c) except with the added multiple nucleation possibility. Once again a single step is produced with the same qualitative features as before, but the elbow of the jump is sharper than before, more in accord with the data curves. As the sample thickness and relative spring strength are reduced, two- and three-layer events appear as in Figs. 16 and 17, in accord with the data. Once again the qualitative features are correct. Between each layer event there is a slowing in the displacement rate, which still remains much greater than the initial and final rates. The overall rate of successive events drops much faster than the total force itself. In esssence, what is occurring is that, due to the multiple nucleations, if the relative spring strength is weak enough, after the first layer event the sample thickness will change by slightly more than one layer. The compression on the singly nucleated portions in the center of the sample will then be greater than it was initially, and the second layer event occurs rapidly on the heels of the first. Once again multiple nucleations are possible, but the probability is nearly zero that those portions of the droplet, where the compression has already been relieved by more than one layer, will undergo any nucleation. These two effects balance out, and overall only one layer is removed from the sample on this second jump. Meanwhile, the spring continues to lower the total force and, thus overall, the compression on each screw dislocation. This in turn drops the rate at which nucleations and therefore each successive jump takes place.

2. Dynamic growth simulation

The main difficulty with these model results for multistep events is the relative time scales of the subsequent steps. If the parameters are set such that the last jump occurs in a time comparable to that of the experimental data, then the initial step tends to occur an order of magnitude or more faster than

TABLE III. Summary of computer models.

Model	Line nucleation	Line growth	Characteristics
Edge dislocation (Sec. IV A)	above threshold stress, and unpinning of existing edge dislocations	stress and size dependent	poor agreement with experiment: shape monotonically decreasing relaxation, size unrelated to layers
Static screw dislocation (Sec. IV C 1)	latent SDLs[a] at lattice sites; dependent on Boltzman factor	instantaneously fill unit cell	good qualitative fit to single-layer events, no multilayer events
Static screw dislocation, with multiple nucleation (Sec. IV C 1)	latent SDLs[a] at lattice sites; dependent on Boltzman factor + ~10% chance of multiple nucleations	instantaneously fill unit cell	good qualitative fit to single-layer and multilayer events, rate of successive events vary perhaps too greatly with force
Dynamic growth (Sec. IV C 2)	latent SDLs[a] at lattice sites; dependent on Boltzman factor + ~10% chance of multiple nucleations	dependent on size and stress until pinned	good qualitative fit to single-layer events, rate of successive events varies too little with force
Dynamic growth with continuous generation Sec. (IV C 3)	constant SDL[a] density; Boltzman factor +~10% as above, primary: at lattice sites, secondary: outside primary radius	primary: dependent on size and stress until pinned secondary: no growth, nucleation area added to primary area	good qualitative agreement with single- and multilayer events

[a]SDL: screw dislocation line

expected from the data. Of course, considering the strong dependence of the simulations on the shape and size of the liquid crystal sample, and considering that in the actual experiment the regions of well-ordered smectic A in all probability follow some type of noncontinuous distribution, such discrepancies are perhaps to be expected. However, it also seems probable that assuming helices are immediately pinned after nucleation and ignoring their growth rate is too extreme. Therefore to include helix growth in the growth dynamics the so called pinning radius is made greater than the nucleation radius. Then after nucleation the helix is allowed to grow to $r_{\max}$ in accord with Eq. (4.5). This, of course, brings up the problem, ignored until now, of exactly what the nucleation radius (r_n) should be, which is solved by the following simplifying assumption. An examination of the total energy curves that exist when typical nucleations occur reveals that $W_{\max}$ is located at approximately $r=(D\lambda)^{1/2}$. Further, the energy drops by k_BT at $\sim 1.2r$. So for the simulation, T_l in Eq. (4.5) is adjusted to produce $dr/dt=0$, $v=0$ at $r=(D\lambda)^{1/2}$ and r_n is therefore taken in the range $r<r_n<1.2r$. The results are not dependent on r_n within this range. At a thickness of 1 μm this gives an $r_n\sim 26$ nm, and at 100 μm, $r_n\sim 260$ nm. Once again, in these simulations the largest effect appears to come from the shape and size of the droplet. A typical simulation carried out under the above assumptions is shown in Fig. 17(a). In certain respects the correspondence to the experimentally observed data is improved, but in one important respect the result is disappointing. On the improved side, the ending of each layer step is less sharp and the pseudopauses between layer events are more prominent. However, the rapidity of each step now is roughly the same, varying much too linearly with the total force. In essence, the initiation of each layer event still depends on the nucleation probability, but the dynamics is determined by the growth rate of relatively large helices, which approaches a linear function of stress.

3. Screw dislocation continuous nucleation simulation

Thus, some middle course between a pure nucleation model and one dominated by growth after nucleation is needed. One possibility is to drop the assumption of preexisting or latent screw dislocations in the sample and replace it with a continuous nucleation model. In other words, at any particular time the number and distribution of screw dislocation lines would depend on some probability per unit area of liquid crystal, which would then be combined with the helix nucleation probability. In such a model if the screw dislocation probability per unit area is relatively high, then the pure nucleation model above will be eventually reproduced, whereas at low probabilities the results should be more like those of Sec. IV C 1. To rigorously carry out this type of simulation requires a much more detailed understanding of screw dislocations and their generation. However, a rough approximation to this type of model has been attempted. In this variation the nucleation probability at a lattice site is multiplied by an assumed number of screw dislocation lines within the pinning radius. Two factors next govern the subsequent growth of the helix. First there is the normal growth of Eq. (4.5) and second there is growth due to ''secondary'' nucleations. These nucleations differ from the ''primary'' nucleations that continue to be allowed at the lattice site in that they are assumed to occur outside of the helix radius. Inside the helix the compression has been reduced by a layer and the probability of another nucleation is small until the displacement also changes by a layer. On the other hand, outside the helix no such decompression has occurred and the nucleation probability is higher than ever. These secondary nucleations are accounted for in only the most approximate manner. Their number is taken to be equal to the product of the area within $r_{\max}$ but outside of r, a set number of screw dislocation lines per unit area, and the helix probability. After their ''nucleation'' no attempt is made to keep track of individual growth rates; instead, the size of the pri-

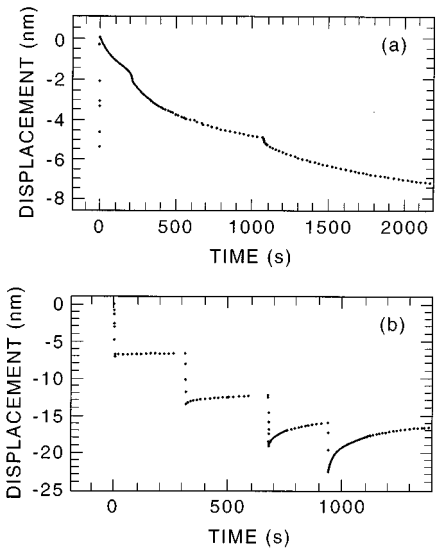

FIG. 18. (a) Relaxation event at 29 °C and $D_0 \cong 1.5\ \mu$m, and (b) series of dilative steps at 31 °C and $D_0 \cong 1.5\ \mu$m.

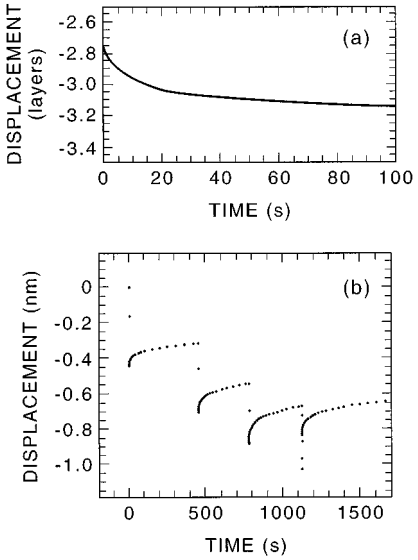

FIG. 19. (a) Simulated relaxation with a relative stiff spring of $k_{sp}/k_{LC}=0.35$ and MNP=11.25%, $\rho_{min}=1.0$ mm, $\rho_{max}=2.0$ mm, $D_0=4.0\ \mu$m (no dynamics), (b) series of dilative experimental steps with spring constant≅5 times that of liquid crystal.

mary helix is merely increased to account for the nucleated area. Even with all these approximations, and hopefully not because of them, comparing Fig. 17(b) to Fig. 11(e) demonstrates that the model produces simulations reasonably close to the experimental data. A summary of the various computer models is presented in Table III.

V. PLASTIC FLOW VIA EDGE DISLOCATIONS

We have shown that the primary yield mechanism in samples of around a micron or more thickness is the helixing of ubiquitous screw dislocation lines. One anticipates, however, that as the sample thickness is decreased, eventually the stress-mediated unpinning and direct nucleation of edge dislocations will come to dominate the dilation-mediated helical instability of screw dislocations. For instance, decreasing the sample thickness an order of magnitude from 4 μm–0.4 μm changes only the dilation required to helix a screw dislocation from around 2.6 layers to 2 layers. Meanwhile, the stress required to produce this dilation will have increased by a factor of 8. A clear signal of this transition with a crossed cylindrical surface geometry is not expected since the outer portions of the sample, where the surfaces may be several microns apart even when $D_0=0$, support the majority of the force. However, it is still interesting to ask at what separation distance this transition is expected to take place. Naturally, any pinned dislocations in the liquid crystal can serve as nucleation sources and will increase the transition thickness. However, a theoretical minimum thickness can be estimated by assuming an edge dislocation-free smectic A. In that case the energy (E) required to produce a new edge dislocation [32] is $E=-b\sigma\pi r_e^2+\gamma 2\pi r_e$. The maximum or activation energy (E_{max}) for the nucleation of the dislocation is then

$$E_{max}=\pi\frac{\gamma^2}{b\sigma}=\pi\frac{\gamma^2 D}{bBa}.$$

Such nucleations will become a significant factor when

$$\frac{1}{\tau}\exp\left(\frac{E_{max}}{kT}\right)\sim 1/\text{sec},$$

$1/\tau$ being a typical molecular frequency $\sim 10^{12}$ s. Assuming γ is comparable to the splay elastic constant $K \cong 10^{-6}$ dynes, using the other parameters listed for 8CB, and setting a to the dilation necessary to induce a helical instability ≅2 layers; one finds a transition thickness $D_{tr} \cong 0.1\ \mu$m.

Plastic flow via screw dislocation helixing is observed well away from the nematic to smectic—A phase transition temperature. This is a second order, or very weakly first order, phase transition in 8CB, and probing closer to it is an obvious extension of this work. Preliminary investigations show, as is to be expected, that the force taken to induce plastic flow drops to zero as the phase transition temperature is approached; however, they also indicate that the character of the relaxation process fundamentally changes. Figure 18(a) shows a relaxation event measured at 29 °C, or roughly 2.5 °C below the transition temperature. The speed of the relaxation is significantly slower than most of those in Sec. III, and the prominent lower temperature single-layer jumps seem to have become small protuberances on a smooth slowly decaying slope although they are still separated by approximately 3 nm. Figure 18(b) shows a series of dilative steps taken at a temperature of 31 °C, or only 0.5 °C from the transition temperature. Here the relaxations have become just a smooth, slowly decaying slope with all vestiges of layer jumps completely hidden.

It may be more than coincidence that Fig. 18(b) is reminiscent of the edge dislocation model results pictured in Fig. 12. As the temperature rises it is not unreasonable to suppose that the effect of pinning will wane, and the transition to edge dislocation mediated flow may begin. Flow in the high stress central region of the liquid crystal droplet would then come to be dominated by edge dislocation movement whereas the remainder of the sample would still respond to

helical instabilities. As the temperature continues to approach the phase transition, more of the droplet would undergo flow from the edge rather than screw dislocations and the relaxation should come to look more like those predicted by the edge dislocation model. On the other hand, the screw dislocation model predicts significant variations depending on the size and shape of the droplet. Furthermore, the lower yield force needed at these higher temperatures means that the strength of the top surface spring is stronger compared to the liquid crystal. This in itself can serve to slow down and stop a cascade of instabilities. For instance, Fig. 19 shows a simulated event with $k_{sp}/k_{LC}=0.35$. Also Fig. 19 shows what happens at 29 °C when the electrostatic servo is set to effectively increase the spring constant to $\cong 5$ times that of the liquid crystal. The series of steps once again shows none of the layering artifacts.

ACKNOWLEDGMENT

This work was supported by an NSF Solid State Chemistry Grant No. DMR 96-14061.

[1] P. G. de Gennes and J. Prost, *The Physics of Liquid Crystals* (Clarendon, Oxford, 1993).
[2] R. G. Horn, J. N. Israelachvilli, and E. Perez, J. Phys. (France) **42**, 39 (1981).
[3] P. Kekicheff and H. K. Christenson, Phys. Rev. Lett. **63**, 2823 (1989).
[4] P. Richetti, P. Kekicheff, J. L. Parker, and B. W. Ninham, Nature (London) **346**, 252 (1990).
[5] O. Abillon and E. Perez, J. Phys. (France) **51**, 2543 (1990).
[6] J. N. Israelachvili, *Intermolecular and Surface Forces* (Academic, London, 1992).
[7] D. Davidov, C. R. Safinya, M. Kaplan, R. Schaetzing, R. J. Birgenau, and J. D. Litster, Phys. Rev. B **19**, 1657 (1979).
[8] L. Bourdon, M. Kleman, L. Lejcek, and D. Taupin, J. Phys. (France) **42**, 261 (1981).
[9] P. Oswald and M. Kléman, J. Phys. (France) Lett. **45**, 319 (1984).
[10] W. I. Glaberson, W. W. Johnson, and R. M. Ostermeir, Phys. Rev. Lett. **33**, 1197 (1974); R. M. Ostermeir, and W. I. Glaberson, J. Low Temp. Phys. **21**, 191 (1975).
[11] J. R. Clem, Phys. Rev. Lett. **38**, 1425 (1977).
[12] J. N. Israelachvilli, J. Colloid Interface Sci. **44**, 259 (1973); D. Tabor and R. H. S. Winterton, Proc. R. Soc. London, Ser. A **312**, 435 (1969).
[13] A. Tonck, J. M. Georges, and J. L. Loubet, J. Colloid Interface Sci. **126**, 150 (1988).
[14] R. Herke, Ph.D. thesis, Department of Physics, University of Colorado, 1993.
[15] A. L. Hugill, J. Phys. E **15**, 597 (1982).
[16] R. V. Jones and J. C. S. Richards, J. Phys. E **6**, 589 (1973).
[17] P. P. Karat and N. V. Madhusudana, Mol. Cryst. Liq. Cryst. **36**, 51 (1976).
[18] N. A. Clark and R. B. Meyer, Appl. Phys. Lett. **22**, 493 (1973).
[19] R. Ribotta and G. Durand, J. Phys. (France) **38**, 179 (1977).
[20] R. B. Meyer, B. Stebler, and S. T. Lagerwall, Phys. Rev. Lett. **41**, 1393 (1978).
[21] L. Ricard and J. Prost, J. Phys. (France) **42**, 861 (1981).
[22] J. Weertman and J. Weertman, *Elementary Dislocation Theory* (Macmillan, New York, 1964).
[23] M. Kléman, J. Phys. (France) **35**, 595 (1974).
[24] L. Bourdon, 3rd Cycle Thesis, Universite de Paris VII, Orsay (1980).
[25] M. Kléman, C. Williams, J. Costello, and T. Gulik-Krzywicki, Philos. Mag. **35**, 33 (1977).
[26] P. S. Pershan, J. Appl. Phys. **45**, 1590 (1974).
[27] P. Oswald and M. Kléman, J. Phys. (France) Lett. **43**, L411 (1982).
[28] P. S. Pershan and J. Prost, J. Appl. Phys. **46**, 2343 (1975).
[29] F. R. N. Nabarro, *Theory of Crystal Dislocations* (Dover, New York, 1967).
[30] P. Oswald, C. R. Seances Acad. Sci. II, Mech.-Phys. Chim. Sci. Terre Sci. Universe **296**, 1385 (1983).
[31] J. Friedel, Dislocations (Pergamon, Oxford, 1964).
[32] Orsay Group on Liquid Crystals, J. Phys. (France) Colloq. **36**, C1 (1975).